Geophysical Journal International

Geophys. J. Int. (2017) **208,** 992–1008
Advance Access publication 2016 November 22
GJI Seismology

doi: 10.1093/gji/ggw438

The 2015 April 25 Gorkha (Nepal) earthquake and its aftershocks: implications for lateral heterogeneity on the Main Himalayan Thrust

Ajay Kumar,[1,*] Shashwat K. Singh,[1] S. Mitra,[1] K.F. Priestley[2] and Shankar Dayal[3]

[1]*Department of Earth Sciences, Indian Institute of Science Education and Research Kolkata, Mohanpur* 741246*, West Bengal, India. E-mail: supriyomitra@iiserkol.ac.in*
[2]*Bullard Laboratories, Department of Earth Sciences, University of Cambridge, Cambridge* CB3 0EZ*, United Kingdom*
[3]*Bihar State Disaster Management Authority, Patna* 800001*, Bihar, India*

Accepted 2016 November 17. Received 2016 November 15; in original form 2016 June 24

SUMMARY

The 2015 Gorkha earthquake (M_w 7.8) occurred by thrust faulting on a ∼150 km long and ∼70 km wide, locked downdip segment of the Main Himalayan Thrust (MHT), causing the Himalaya to slip SSW over the Indian Plate, and was followed by major-to-moderate aftershocks. Back projection of teleseismic *P*-wave and inversion of teleseismic body waves provide constraints on the geometry and kinematics of the main-shock rupture and source mechanism of aftershocks. The main-shock initiated ∼80 km west of Katmandu, close to the locking line on the MHT and propagated eastwards along ∼117° azimuth for a duration of ∼70 s, with varying rupture velocity on a heterogeneous fault surface. The main-shock has been modelled using four subevents, propagating from west-to-east. The first subevent (0–20 s) ruptured at a velocity of ∼3.5 km s^{-1} on a ∼6°N dipping flat segment of the MHT with thrust motion. The second subevent (20–35 s) ruptured a ∼18° W dipping lateral ramp on the MHT in oblique thrust motion. The rupture velocity dropped from 3.5 km s^{-1} to 2.5 km s^{-1}, as a result of updip propagation of the rupture. The third subevent (35–50 s) ruptured a ∼7°N dipping, eastward flat segment of the MHT with thrust motion and resulted in the largest amplitude arrivals at teleseismic distances. The fourth subevent (50–70 s) occurred by left-lateral strike-slip motion on a steeply dipping transverse fault, at high angle to the MHT and arrested the eastward propagation of the main-shock rupture. Eastward stress build-up following the main-shock resulted in the largest aftershock (M_w 7.3), which occurred on the MHT, immediately east of the main-shock rupture. Source mechanisms of moderate aftershocks reveal stress adjustment at the edges of the main-shock fault, flexural faulting on top of the downgoing Indian Plate and extensional faulting in the hanging wall of the MHT.

Key words: Earthquake source observations; Seismicity and tectonics; Continental margins: convergent; Asia.

1 INTRODUCTION

The M_w 7.8 Gorkha (Nepal) earthquake on 2015 April 25 initiated ∼80 km northwest of the capital city of Katmandu and ruptured ∼150 km of the frictionally locked downdip segment of the Main Himalayan Thrust (MHT) beneath the central Nepal Himalaya (Avouac *et al.* 2015). The earthquake resulted in ∼4 m of average slip of the Himalayan Mountains over the Indian Plate in the SSW direction (Mitra *et al.* 2015). The main-shock fault spanned between the meisoseismal zone of the 1505 ($M_w > 8.5$) earthquake to its west (Kumar *et al.* 2006) and the rupture zone of the 1934 (M_w 8.2–8.4) Nepal earthquake to its east (Bilham & Wallace 2005; Sapkota *et al.* 2013). The last known great earthquake in this region of Nepal occurred in 1833 (M ∼7.5) (Ambraseys & Douglas 2004) and has a significant overlap with the rupture area of the Gorkha main-shock (Adhikari *et al.* 2015). The main-shock was followed by a series of moderate-to-strong aftershocks, the largest one (M_w 7.3) occurred 18 d after the main-shock, on 2015 May 12 (Fig. 1). Albeit the loss of life and property inflicted by this damaging earthquake and its aftershocks, it has provided an unprecedented opportunity to study the source properties of Himalayan mega-thrust earthquake and its relationship to the geometry of the MHT, which, so far, is poorly understood.

Images of the rupture process by back-projecting teleseismic *P*-waves using single array (Avouac *et al.* 2015), multiple arrays (Zhang *et al.* 2016) and a distribution of stations at a range

*Now at: Group of Dynamics of the Lithosphere (GDL), Institute of Earth Sciences Jaume Almera – CSIC, Barcelona, Spain.

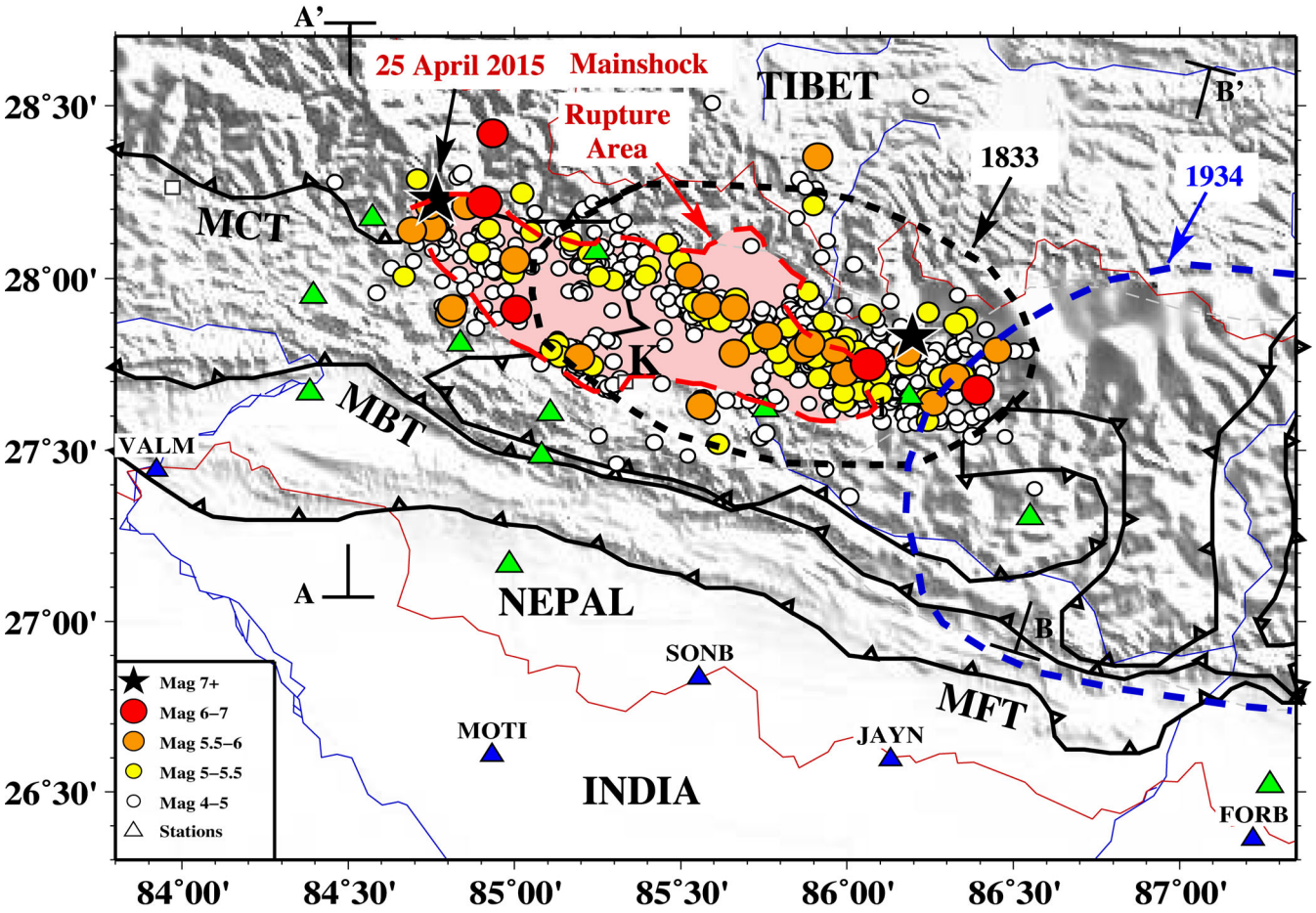

Figure 1. Topographic map of Nepal Himalaya with plot of epicentres of the 2015 April 25 main-shock and aftershocks ($M_w \geq 4.0$) taken from the Nepal DMG catalogue (colour coded and scaled by size—see inset). The rupture areas of the main-shock from Elliott *et al.* (2016) is plotted as a pink patch bound by red dashed line. Approximate rupture area of historical earthquakes of 1833 and 1934, which occurred in Nepal, are plotted as dashed ellipses. Structural elements: MFT, Main Frontal Thrust; MBT, Main Boundary Thrust; and MCT, Main Central Thrust have been adopted from Monsalve *et al.* (2006). Katmandu is marked K and the profiles plotted in Fig. 9 are marked A–A′ and B–B′. Broad-band seismograph stations deployed in India (blue) and Nepal (green), following the main-shock, are plotted as triangles.

of backazimuth and distance (Fan & Shearer 2015) have consistently revealed that the faulting initiated to the west of Katmandu and propagated eastward by ∼140 km. However, significant variations in the details of the rupture process, ranging from linearly distributed high-frequency sources with constant rupture velocity (Avouac *et al.* 2015; Meng *et al.* 2016), to multistage rupture (Fan & Shearer 2015), and depth dependent variation in rupture velocity (Zhang *et al.* 2016) have been reported. Joint inversion of teleseismic waves, strong ground motion data, high-rate and static GPS data and SAR imagery (Galetzka *et al.* 2015; Grandin *et al.* 2015) pointed to a simple unilateral rupture with steady rupture velocity. The downdip limit of the rupture has been conjectured to coincide with the junction between the frontal flat and deeper steeply dipping ramp on the MHT. Geodetic data combined with geologic, geomorphological and geophysical analysis (Elliott *et al.* 2016) revealed that the main-shock slip occurred on the shallow flat portion of the MHT, between 5 and 15 km, and did not require any out-of-sequence thrusting. Study of aftershock distribution (Adhikari *et al.* 2015) highlighted three distinct southward extending belts of seismicity, reflecting possible regions of stress concentrations following the main-shock rupture.

These studies have provided valuable understanding of the main-shock rupture duration and propagation, and high-frequency energy release and slip distribution on the main-shock fault. However, these have been performed for fixed orientation of the fault and are therefore insensitive to the lateral variation in the geometry of the fault plane and asperities on the ruptured segment of the MHT. Given this background, we analysed high-frequency broad-band seismological data to unravel the spatiotemporal variation in the rupture process of the main-shock and the largest (M_w 7.3) aftershock. Results from this analysis are used to parameterize the main-shock and the largest aftershock faults as propagating line sources and modelled by inverting teleseismic body waveforms. The observed misfit to the main-shock high-frequency body waveforms and the heterogeneity observed from the spatiotemporal variation in the rupture process, prompted us to further subdivide the main-shock fault into four segments. These segments were modelled as multiple centroid subevents to highlight possible lateral variations in the fault surface. Additionally, six aftershocks ($M_w > 5.0$), originating at the edges of the main-shock and largest aftershock rupture areas, have been modelled using centroid moment tensor (CMT) inversion. Results of our study provide (i) the first evidence of lateral variation in the structure of the ruptured segment of the MHT; (ii) plausible explanation for the observed spatiotemporal variation in the main-shock rupture velocity and arrest of the rupture to the east, and (iii) the geometric and kinematic relationship between the main-shock, the largest aftershock and moderate-to-large aftershocks.

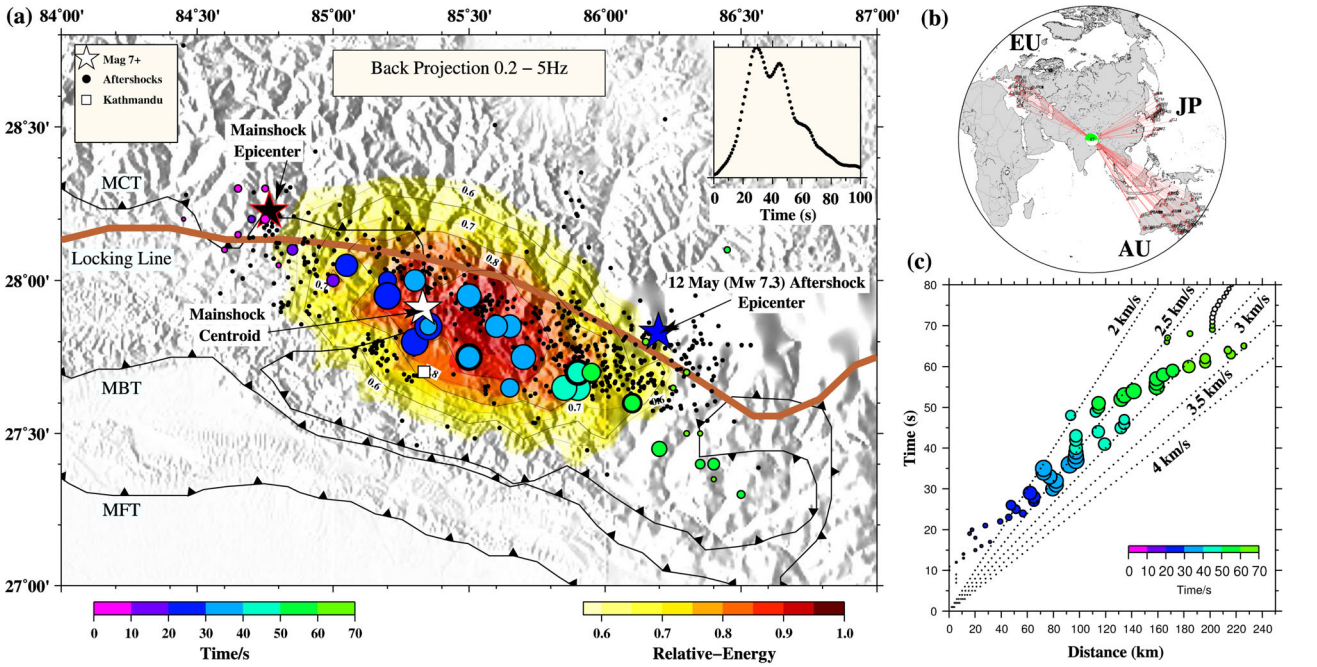

Figure 2. (a) Plot of *P*-wave high-frequency (0.2–5.0 Hz) back projection result for the Gorkha main-shock. The relative energy released from the main-shock is contoured and colour coded to highlight the ruptured area on the fault. The epicentre and centroid location of the main-shock are plotted as black and white stars, respectively. The rupture propagated eastwards and the maximum energy released surrounding the centroid location. The points of maximum amplitude release during faulting are marked by circles scaled by size, denoting relative amplitudes, and colour coded by time delay following the initiation of the rupture. The integrated source time function is plotted in the inset and highlight a multiphase rupture. The points of maximum amplitude occur north of Katmandu (white square) and matches well with the maximum energy contours. (b) Map of stations of the Australian, European and Japanese networks from which teleseismic data has been used for the high-frequency back projection study. The mechanism for the main-shock is plotted at the epicentral location and source–receiver ray paths plotted as red lines. (c) Plot of rupture velocity corresponding to the points of maximum amplitude release shown in (a). Distribution of these points on map and the variation of the rupture velocity points to heterogeneous rupture propagation.

2 BACK-PROJECTION USING MULTIPLE TELESEISMIC ARRAYS: GORKHA MAIN-SHOCK AND LARGEST AFTERSHOCK

Broad-band teleseismic waveform data from the (a) Australian network (76 stations), (b) Japanese network (20 stations) and (c) European network (21 stations) (Fig. 2b) have been used to image the rupture process of the Gorkha main-shock and the largest (M_w 7.3) aftershock, using high-frequency back projection of *P*-wave. The three networks (referred to as arrays henceforth) chosen for this analysis, lie within an epicentral distance range of 30°–90°, and provide a good backazimuthal coverage. The chosen range of epicentral distance is required to avoid waveform complexities at short distances from crust and upper mantle heterogeneities and at long distances from the core-mantle boundary. Additionally, multiple arrays at a range of distances and backazimuths reduces the swimming artefacts introduced due to small aperture of a single array and enhances the lateral resolution of the solution (Kiser *et al.* 2011). Vertical component waveform data have been used for our analysis. The data analysis is done following the procedure outlined in Kiser & Ishii (2012). Waveform data is filtered between 0.2 and 5 Hz, to utilize a broad band of frequencies for the study of rupture time history of the earthquakes. The low- and high-frequency corners at 0.2 and 5 Hz, respectively, provide a broader band than all previous studies (Avouac *et al.* 2015; Fan & Shearer 2015; Grandin *et al.* 2015; Yagi & Okuwaki 2015) and contain information necessary to understand the detailed spatiotemporal variation of the rupture process. The steps of our analysis are briefly outlined below. Further details of the methodology can be found in Kiser & Ishii (2012).

(1) The source region, surrounding the hypocentre is parameterized as a horizontal plane with 0.5° by 0.5° square grids. The plane is fixed in space at the hypocentral depth.

(2) The teleseismic *P*-wave, from each station within the array, is windowed 30 s before and 150 s after the theoretical arrival time computed using the IASP91 velocity model (Kennett & Engdahl 1991).

(3) Within a given array, the windowed *P*-waves are cross-correlated with a reference station (chosen at the centre of the array) to estimate the time shift required to account for the 3-dimensional variation in the velocity structure.

(4) Each grid point on the parameterized hypocentral plane is assumed as a potential source and the travel time of *P*-wave is calculated, using IASP91 velocity model, to all the stations within the array.

(5) Waveforms from these stations, adjusted by the respective time shifts (computed from cross-correlation), are stacked together, starting from the calculated *P*-wave arrival time for a given source grid. During stacking, the waveforms are weighted (i) inversely by the density of stations within an array and (ii) by the cross-correlation coefficient (obtained above).

(6) The weighted stacked energy is then back projected onto the source grid. This procedure is repeated for all potential source grids, for every array.

(7) Information from all the arrays are combined by following a weighting procedure, where the stack from the hypocentral grid is cross-correlated for each array, with respect to a chosen reference array. In our analysis, we used the Australian network as our reference array, as it has the maximum number of stations with a wide aperture.

(8) For every potential source grid, stacked waveforms from each array are adjusted by the estimated time shift and summed by normalizing the amplitude.

(9) For removing the high-frequency artefacts in the stacked waveform at each potential source grid, a 10 s moving average time window is applied. In order to test the influence of the moving average time window on the final result, we performed our analysis for 5, 10, 15 and 20 s time windows. It was observed that the 10 s window is optimal in removing unwanted high-frequency artefacts, while preserving the necessary details of the source time function (STF).

(10) The final distribution of relative energy released during the rupture is contoured on the parameterized hypocentral plane and the points of maximum energy release at each time sample (i.e. 1 s) is highlighted by a circle, whose radius is scaled by the relative amplitude (Fig. 2a, Supporting Information Movie S1 and Fig. S2). The contour plot of energy is truncated at ∼50 per cent of the total energy level, to match the scaled fault area estimated from previous study (Mitra *et al.* 2015).

The results of our analysis reveal that the main-shock ruptured a fault ∼150 km long by ∼70 km wide and occurred over a duration of ∼70 s. The STF has three pulses with peaks at ∼30, ∼45 and ∼60 s. The initiation of the rupture, in the first ∼10 s, is marked by a gradual rise in the STF. This was also observed in the dynamic rupture study of the main-shock using depth phase corrected source spectra for a circular crack model (Denolle *et al.* 2015). The major energy release during the earthquake occurred within 30–50 s of the rupture process. The earthquake initiated at the western edge of the ruptured zone, close to the locking line highlighted by microseismicity over the past decade (Ader *et al.* 2012), and propagated eastward. The multi-pulsed STF is observed to be associated with time dependent rupture velocity (Fig. 2c). Very slow velocity of rupture is observed in the first ∼10 s, which corresponds to the growth of the fault rupture area around the hypocentre. Once the rupture reached a critical area, it propagated eastwards at an average speed of ∼3.5 km s^{-1}, between 10 and 20 s. Following this it slowed down to ∼2.5 km s^{-1} between 20 and 35 s. Beyond 35 s and upto 60 s the rupture velocity increased steadily to reach ∼3.5 km s^{-1}. After 60 s the rupture split into two segments, one propagating southeastward and the other rupturing a region further to the north. Similar rupture-time history and variation in rupture velocity of the main-shock has also been observed using a distribution of stations (Fan & Shearer 2015) and highlights the presence of lateral heterogeneity on the faulted surface. The points of maximum energy released on the fault (marked by circles in Fig. 2a) are aligned along an average azimuth of ∼117°, in agreement with the direction of observed rupture propagation (Supporting Information Movie S1), with higher order deviation from a linear source, pointing to a heterogeneous rupture process. Most of the observed high-frequency (0.2–5 Hz) energy was released north of Katmandu, and is consistent with the slip inversion study of Avouac *et al.* (2015). The cumulative energy distribution on the main-shock fault is bound to the west by its epicentre, and to the east by the largest aftershock (M_w 7.3), which occurred on 2015 May 12.

High-frequency (0.5–2 Hz) back projection result of the largest aftershock show that it originated in the intervening patch of the last stage main-shock rupture, and occurred unilaterally in a single pulse STF of 40 s duration. The rupture initiated in the NNW, close to the downdip edge of the locked zone and propagated updip in the SSE direction at an azimuth of ∼150°. The rupture velocity steadily increased from ∼2 km s^{-1}, in the first 10 s, to ∼3 km s^{-1} between 10 and 40 s. Maximum energy was releases between 20 and 40 s of the rupture process (Supporting Information Fig. S3). Our results corroborate the depth dependent variation in rupture speed observed for this aftershock from the multiarray back projection study of Zhang *et al.* (2016).

3 SOURCE MECHANISM OF THE GORKHA MAIN-SHOCK

The CMT solution for the main-shock given by Global-CMT and USGS are very similar, showing a predominantly thrust fault on a shallow NE dipping plane. The centroid location is ∼80 km east of the epicentre, attesting to the eastward propagation of the rupture (Fig. 2a). We forward calculated synthetic long-period (15–100 s) seismograms at teleseismic distances (30°–90°) for both these source mechanisms and found significant misfit to the observed waveforms (Fig. 3). This prompted us to model the source mechanism of the main-shock using moment tensor inversion of long-period teleseismic body waves. First, we modelled the main-shock as a centroid source and observed a poor fit to the long-period waveforms, due to directivity effects, and also to the high-frequency body waves, which contained details of the rupture process (Supporting Information Fig. S4). We then undertook the modelling of the main-shock source as a two-step process: (1) First, we modelled it as a propagating line source using the azimuth of rupture propagation obtained from the back projection result. The point source centroid solution is used as the starting model for the inversion. (2) Second, we subsequently modelled the main-shock as multiple subevents. The parameterization of the subevent faults are done using the multi-pulsed STF and the spatiotemporal variation in the rupture velocity obtained from back projection. The line source solution obtained from (1) above is used as the starting model for the inversion. This two-step approach had been used earlier for the Zirkuh earthquake in Iran and had produced significantly improved results compared to the CMT solution (Berberian *et al.* 1999).

We use high-frequency *P*- and *SH*-waveform data from an epicentral distance range of 30° to 80° recorded at the Global Digital Seismic Network (GDSN) stations for computing the source mechanisms. The 3-component waveform data is deconvolved with the instrument response, and subsequently reconvolved with a filter to reproduce the 15–100 s response of the WWSSN long-period instruments. The horizontal components are rotated using the back-azimuth angle to produce radial and transverse components. The *P*- and *SH*-waveforms are windowed on the vertical and tangential components, respectively. The length of the window is chosen to be of 90 s duration, based on the STF computed from the back projection study (Fig. 2a inset). The windowed waveforms are modelled using the moment tensor inversion algorithm of McCaffrey & Abers (1988).

The details of this methodology has been described in Nabelek (1984); McCaffrey & Nabelek (1987); Berberian *et al.* (1999); Paul *et al.* (2015); Kumar *et al.* (2015) and we will briefly outline the main steps. The algorithm estimates the strike and dip of the nodal plane(s), rake of the slip vector(s), centroid depth, and the variation of moment release with time (the STF). The time integral of the STF gives the seismic moment. The final solution is obtained by minimizing the least square misfit between the observed and the synthetic *P*- and *SH*-waveforms, using an iterative approach. The synthetic waveform is computed for a given double couple source embedded in a simple Earth structure, by convolving the STF with the computed Greenś functions for direct arrivals (P or S), near-source

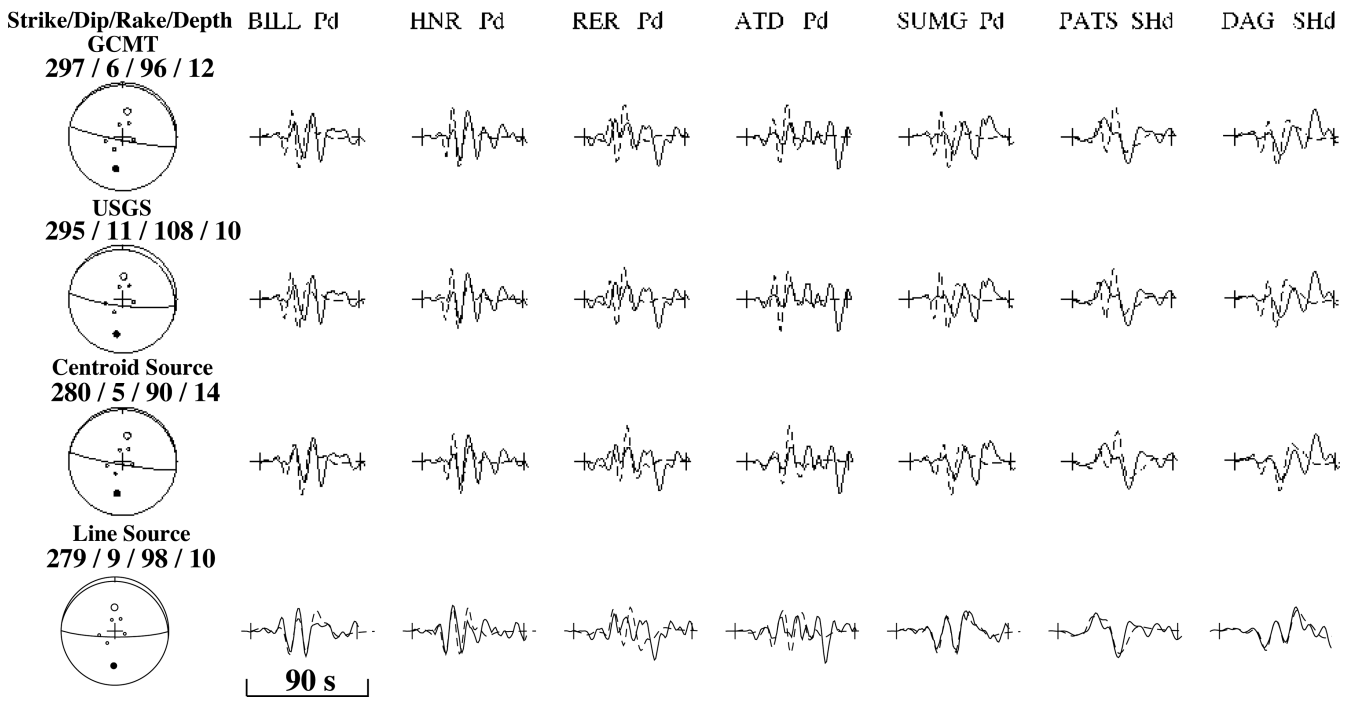

Figure 3. A comparison between observed (solid) and synthetic (dashed) waveform fit for the GCMT, USGS centroid, inversion using centroid source (this study) and inversion using line source oriented 117° and propagating with velocity 2.3 km s^{-1} (this study). A significant improvement in the fit to the long-period waveform is observed for a line source with directivity compared to the centroid source. However, the high-frequency, low-amplitude arrivals in the first ∼20 s and 60–90 s of the *P*-waveforms are poorly fit. Length of the plotted waveform is 90 s.

reflections (pP, sP or sS) and multiples. As the waveform amplitude and shape are nonlinearly related to the source parameters, the source parameters are iteratively perturbed towards minimizing the misfit. The STF is defined using a series of overlapping isosceles triangles of fixed half-width duration. For the source region we chose a velocity model based on previous studies (Monsalve *et al.* 2006; Nábělek *et al.* 2009). The observed and synthetic waveforms are aligned by precisely reading the *P*-wave arrival time from the broad-band record. The *SH*-waveform is weighted half the *P*-waveform due to its larger amplitude, and all observed seismograms are azimuthally weighted to remove bias from a cluster of stations compared to isolated ones. The best-fitting source parameters are found by minimizing the misfit in amplitude and shape, between the observed and synthetic waveforms for all stations simultaneously.

From the back projection results of the main-shock (Fig. 2a), it is obvious that directivity will have significant effect on the shape and amplitude of the waveforms as a function of the station azimuth. We, therefore, initiated the inversion for a propagating line source with a rupture velocity (V_r) of 2.3 km s^{-1} at an azimuth of 117°. The rupture velocity is obtained as an average for the entire fault and is computed by dividing the along strike length of the rupture area (∼160 km) by the total duration of faulting (∼70 s), estimated from the STF. The rupture azimuth is chosen from the direction of propagation of the high amplitude pulse generation points during the main-shock rupture (Fig. 2a). The half-width of the elements of the STF is chosen to be 4 s, with a total of ten elements. Due to the propagating rupture the apparent STF is compressed or expanded as a function of the station azimuth. The result of the inversion is plotted in Figs 4 and 5, and summarized in Table 1. We observed that the long-period features of the seismograms are well reproduced in the synthetic waveforms. We compare our solution for the line source to the GCMT, USGS and our centroid solutions, by observing the fit to the waveforms (Fig. 3). We choose seven stations to demonstrate the improvement in fit for the line source. These stations are distributed in backazimuth and are either nodal plane stations (in the direction of or away from the rupture) or are perpendicular to the strike of the fault plane. Both, the waveform amplitude fit (stations BILL, HNR, ATD, SUMG, PATS, DAG) and the fit to the width of the pulses (stations BILL, RER, SUMG) show significant improvement for the line source.

Although the line source is an improvement from the centroid source and better fits the long-period amplitude and phase of the waveforms, it is unable to provide a good fit for the high-frequency information present in the first ∼20 s and between 60 and 90 s of the *P*-waveforms. It also overestimates the maximum amplitude in the *P*-waveform between 30 and 40 s. To improve the fit to the data the main-shock is represented by a series of discreet centroid subevents, separated temporally and spatially with a higher frequency STF half-width (2 and 3 s). The choice of the number of subevents and their spatial and temporal spans have been derived from the number of pulses in the STF and the variations in the rupture velocity obtained from back projection. The best fit to the observed waveforms have been achieved with four subevents occurring sequentially from west to east (Figs 6 and 7, and Table 1).

The first 20 s of the waveform, containing low amplitude and high frequencies, is modelled to obtain an M_w 7.2 subevent. For the inversion we use an STF of 20 s duration with high-frequency half-width of 2 s. The fit to the high-frequency *P*-waveform is significantly improved compared to the line source and the waveform polarity tightly controls the initial rupture of the Gorkha main-shock (Supporting Information Fig. S5). This subevent is a thrust fault on a shallow north dipping (∼6°) fault plane with the slip vector pointing south (Figs 6 and 7). The depth of this subevent is ∼15 km, which lies within the uncertainties of the main-shock line source

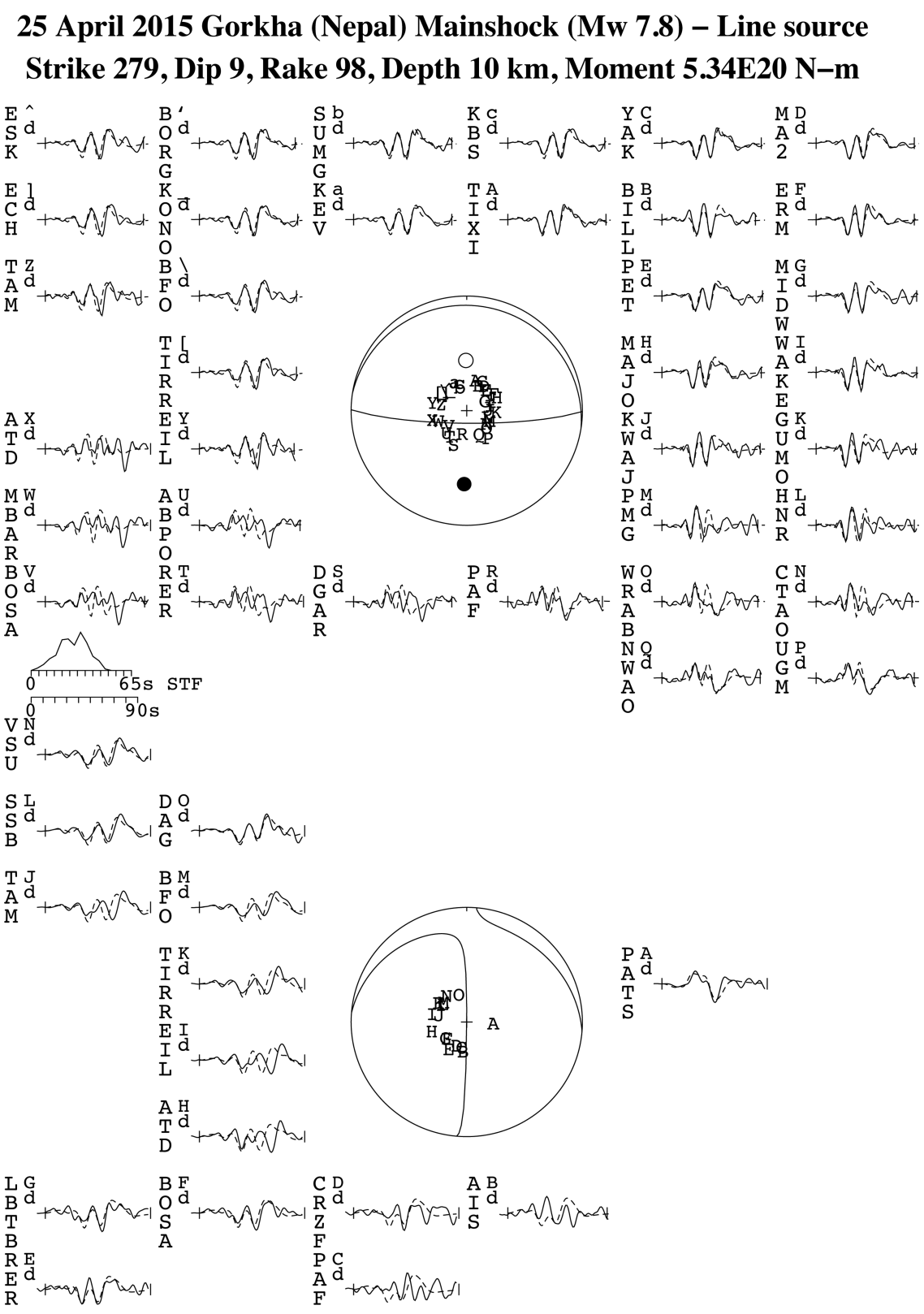

Figure 4. *P* (top) and *SH* (bottom) focal mechanism and waveforms (observed, bold; synthetic, dashed) for our minimum-misfit solution of the Gorkha main-shock, calculated for a line source propagating along azimuth 117° with a velocity of 2.3 km s^{-1}. Source parameters for the best-fitting solution are written on top. The station code for each waveform is accompanied by a letter corresponding to its position in the focal sphere. The time window used for the inversion is marked by vertical lines on each waveform. The pressure and tension axes are plotted as solid and open circles on the *P*-wave focal sphere. The source time function (STF) is plotted as triangular elements.

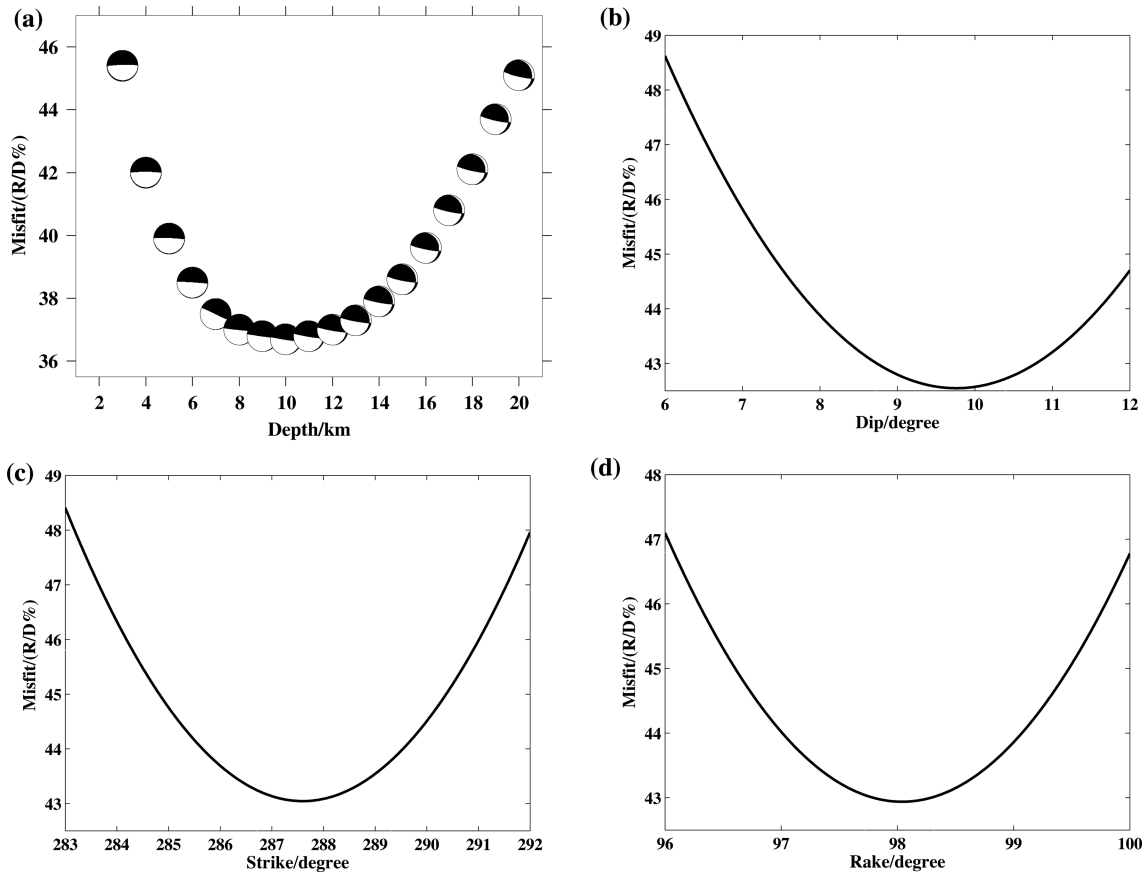

Figure 5. Uncertainty analysis for the focal mechanism parameters of the main-shock line source solution: (a) depth, (b) dip, (c) strike, and (d) rake. To estimate the uncertainty, each parameter is fixed at values surrounding the minimum misfit solution (plotted on the *x*-axis) and all other parameters are allowed to vary freely in the inversion. The misfit value is shows as the percent of the weighted residual variance to the weighted data variance (R/D per cent) on the *y*-axis. To demonstrate the trade-off between the focal mechanism with depth, focal mechanism for every fixed depth is overlay plotted on the misfit curve in (a).

(Figs 4 and 5, Table 1). The high-frequency, low amplitude first ∼20 s pulse from the main-shock faulting matches the slow initiation observed in slip inversion (Avouac *et al.* 2015) and from dynamic modelling (Denolle *et al.* 2015).

The first subevent is then held fixed and we include a second subevent nucleating 20 s after the first one. The STF is extended by 15 s with elements of 3 s half-width duration. The fit to the waveform improves significantly upto 40 s and the inversion yields an M_w 7.3 subevent on an oblique thrust fault dipping at ∼18° to the WNW (Figs 6 and 7). The slip vector for this subevent points to the south. A third subevent is added after 35 s of the first one. The STF is extended by another 15 s, with 3 s half-width elements and the inversion window is increased to 60 s. Inverting the waveform, we obtain an M_w 7.4 subevent on shallow north dipping (∼7°) thrust fault with the slip vector oriented SSW. This subevent is the biggest of the three and fits the largest amplitude arrival between 30 and 60 s. The focal mechanism of the first and the third subevents matches the centroid (Supporting Information Fig. S4) and line source (Fig. 4) solutions. This confirms that the centroid solution is primarily controlled by the amplitude of the initial and the largest arrival on the waveforms and has poor sensitivity on high-frequency phases.

The final segment of the waveform between 60 and 90 s could not be fit with these three subevents and required a fourth subevent at 50 s. The STF is extended by 20 s with elements of 3 s half-width duration. The first three subevents are held fixed and the inversion is performed to fit the waveform upto 90 s. The fourth and final subevent is modelled to be an oblique strike-slip earthquake (M_w 7.3), distinctly different from the first three subevents. Both nodal planes of this subevent are steeply dipping and at high angle to the shallow dipping faults of the first three subevents. Additionally, this subevent has a large strike-slip component. It is possible that the motion on the main fault, which ruptured through the first three subevents, could have been transferred onto an oblique strike-slip structure.

The uncertainties on the modelled parameters are estimated through a number of tests described in details in our previous studies (Kumar *et al.* 2015; Paul *et al.* 2015). We estimate the uncertainty in depth of the main-shock line source solution by fixing the depth of the earthquake to values bracketing the best-fitting solution and reinvert the waveform data for the other focal parameters. This results in a Gaussian distribution of misfit with respect to depth, from which we estimate the 1σ bound on depth. This also reveals the trade-off between depth and other parameters in the focal mechanism (Fig. 5a). We follow the same procedure to estimate the uncertainty in the strike, dip and rake of the best-fitting solution. The 1-σ bounds for the uncertainty on each modelled parameter are abstracted by fitting a Gaussian distribution (Figs 5b–d and listed in Table 1). Similar analysis could not be done to estimate the formal uncertainties for the solutions of the multiple subevents, due to

Table 1. Event date, origin time, location (taken from the catalogue of the Department of Mines and Geology (DMG), Nepal: http://www.seismonepal.gov.np/), magnitude, misfit and best-fitting focal mechanism parameters (depth, strike, dip and rake) with associated uncertainties. The misfit is given as per cent of the weighted residual variance to the weighted data variance (R/D per cent). The $\pm 1\sigma$ uncertainty for the modelled parameters are listed along with. Fixed depth of subevents 2, 3 and 4 are marked with (f). TWI—Teleseismic waveform inversion. The corresponding focal mechanisms are plotted in Fig. 8.

ID	Event date (dd-mm-year)	Origin time (hr:mm:ss)	Lat (°N)	Long (°E)	M_w	Misfit R/D %	Depth (km)	Strike (°)	Dip (°)	Rake (°)	Reference
Main-shock: single source models											
a.	25-04-2015	06:11:24	28.23	84.76	7.8	106.9	14±3	280±3	5±2	90±4	Centroid source (TWI)
						99.6	10±4	279±4	9±4	98±2	Line source (TWI)
Main-shock: multiple source model (4 subevents)											
					7.2		15±2	269	6	72	Subevent-1 (TWI)
					7.3		15(f)	197	18	15	Subevent-2 (TWI)
					7.4		15(f)	308	7	115	Subevent-3 (TWI)
					7.3		15(f)	177	76	19	Subevent-4 (TWI)
Aftershocks											
b.	25-04-2015	06:45:19	28.22	84.90	6.7	–	20	285	7	86	GFZ
c.	25-04-2015	17:42:51	28.35	85.91	5.1	49.6	10±2	259±5	57±2	231±4	Centroid source (TWI)
d.	25-04-2015	23:16:15	27.90	85.00	5.1	82.3	13±3	297±5	78±3	217±5	Centroid source (TWI)
e.	26-04-2015	07:09:09	27.74	86.06	6.9	29.7	14±2	336±4	7±2	134±3	Centroid source (TWI)
f.	26-04-2015	16:26:07	27.81	85.88	5.0	52.2	11±3	230±6	31±4	56±6	Centroid source (TWI)
g.	12-05-2015	07:05:18	27.83	86.19	7.3	19.5	15±2	281±2	7±1	90±2	Centroid source (TWI)
						29.4	14±3	318±5	9±2	121±4	Line source (TWI)
h.	12-05-2015	07:17:19	27.86	86.32	5.5	63.9	13±3	247±3	21±2	62±5	Centroid source (TWI)
i.	12-05-2015	07:36:51	27.67	86.39	6.3	–	15	303	23	123	USGS
j.	16-05-2015	11:34:09	27.63	86.26	5.5	69.4	7±3	288±4	23±3	102±4	Centroid source (TWI)

waveform interference. However, we do a number of forward calculations to establish the validity of our result and obtain insights into the associated uncertainties in the overall solution. For the first subevent, the depth was kept as a free parameter in the inversion and in subsequent subevents, we fix the centroid depth to the best-fitting value obtained from the first subevent. We, therefore, do a depth sensitivity test for the first subevent as outlined above. This produces a 1-σ bound of ± 2 km. Next, we illustrate the sensitivity of the waveform to the source mechanism of the subevents, by sequentially adding them and observing the fit to the waveform from five stations (Fig 7). This confirms the necessity of each subevent in improving the fit to the waveforms. We then replace all the subevents with the centroid solutions and demonstrate that this produces an observable misfit to the waveforms at stations CTAO, GUMO, HNR, PMG and KWAJ. As the last subevent is significantly different in mechanism compared to the first three subevents, so we replace this subevent with a thrust mechanism similar to the third subevent and observe the misfit to the waveforms. This produces observable misfit at stations CTAO, HNR and PMG. Finally, we calculate the cumulative seismic moment released by the four subevents and find it to be equal to the seismic moment of the main-shock, adding up to an M_w ~7.8 earthquake (Fig. 7).

4 SOURCE MECHANISM OF THE AFTERSHOCKS

The source mechanism of larger aftershocks ($M_w > 5.0$) which occurred within a month of the main-shock, have been modelled using the moment tensor inversion technique described in Section 3. The 2015 May 12 (M_w 7.3) largest aftershock has been modelled as a point (centroid) source and as a line source (Supporting Information Figs S10 and S11). For all other aftershocks we assume a point source embedded within a simple structure. The source parameters of the aftershocks are described in time sequence of their occurrence following the main-shock. The uncertainties on the modelled parameters and trade-offs between parameters are estimated through similar tests described in the previous section and tabulated in Table 1.

4.1 2015 April 25 aftershocks

On the same day following the main-shock, there were three major aftershocks, of which the first one is the largest (M_w 6.7) and occurred within ~35 min of the main-shock origin time (event b in Fig. 8 and Table 1). This resulted in the surface waves from the main-shock to contaminate the body wave arrivals of the aftershock at teleseismic distances. We could not model the source mechanism of the aftershock using GDSN data. However, for discussion we include the mechanism given by GFZ. The GFZ source mechanism reveal that this event had a similar mechanism as the main-shock and originated within ~10 km of the main-shock epicentre. The depth of the event is reported as ~20 km, which is slightly larger than the centroid depth of the main-shock. Given the interference from the main-shock surface waves, the depth phase may not have been reliably identified.

The second major aftershock (M_w 5.1) occurred ~11 hr after the main-shock and originated north of the main-shock rupture area (Fig. 8). This earthquake had a predominantly normal fault mechanism and occurred at a depth of ~10 km within the Tethyan Himalaya (Supporting Information Fig. S6 and event c in Fig. 8 and Table 1). Shallow normal faulting earthquakes are common in south-central Tibet (Craig *et al.* 2012), with the fault planes oriented in the N–S direction. However, in this event both the nodal planes are E–W oriented. We interpret this event as a result of post-seismic extension in the back of the overriding wedge, following the southward slip of the Himalaya over the Indian Plate in the main-shock. This is corroborated by geodetic measurements of surface displacement, where an observed subsidence by ~0.6 m occurred

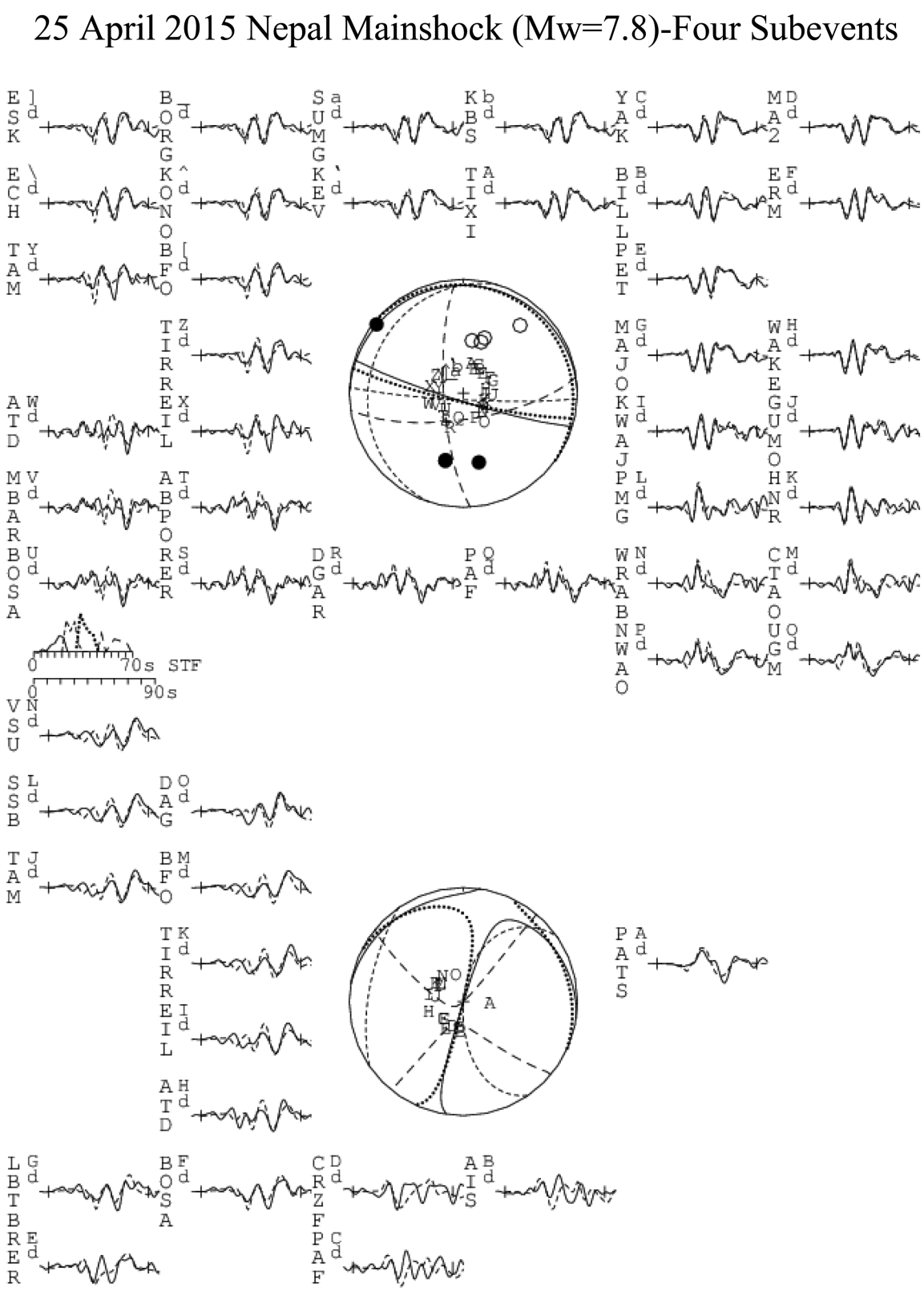

Figure 6. *P*- and *SH*-waveform inversion solution for the Gorkha main-shock using four subevents (Table 1). Plot of nodal planes and STF are shown for subevents 1 (solid), 2 (small dashes), 3 (dotted) and 4 (big dashes). Rest of the figure caption is same as Fig. 3.

in the High Himalaya (Elliott *et al.* 2016) above the hypocentre of this earthquake. Similar extensional faulting has been commonly observed in the hanging wall of subduction megathrust earthquakes (McKenzie & Jackson 2012; Hayes *et al.* 2013).

The third major aftershock (M_w 5.1) occurred ~5.5 hr after the previous one and originated close to the southern edge of the main-shock rupture area (Fig. 8). This event had an oblique normal fault mechanism with a strong strike-slip component and occurred at a

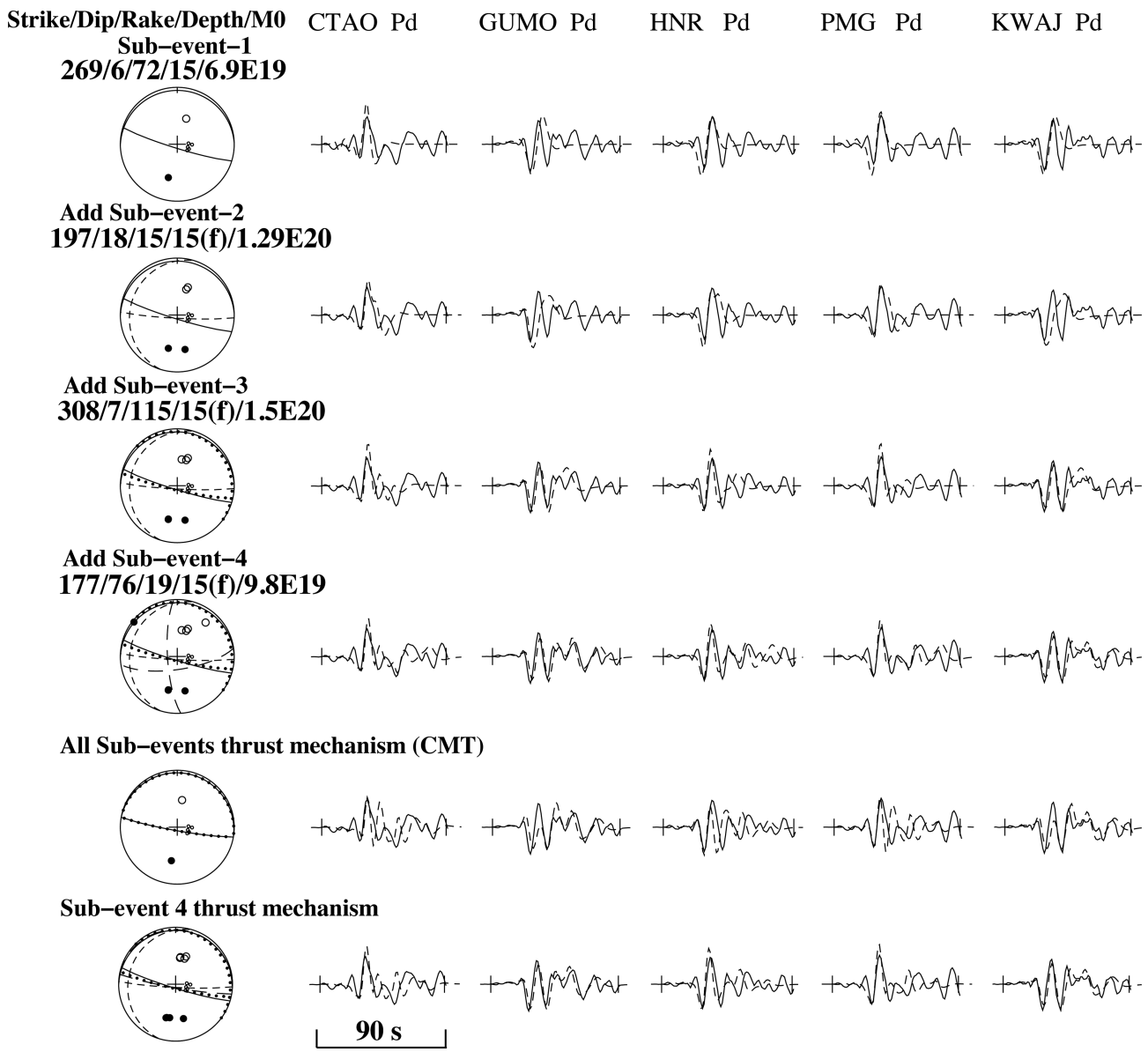

Figure 7. Plot of waveform fit towards constraining the four subevents plotted in Fig. 6. A subset of most sensitive waveforms (*P* and *SH*) has been used for comparison. Top line is the fit for subevent 1 (M_w 7.2) with the corresponding focal mechanism plotted on the left. Observe the fit to the first 20 s low-amplitude, high-frequency waveform (also see Supporting Information Fig. S5). The second line is after adding subevent 2 (M_w 7.3). Observe the improvement of fit upto 40 s. The third line is after adding subevent 3 (M_w 7.4) and fits the large amplitude arrival between 40 and 70 s. The fourth line is after adding subevent 4 (M_w 7.3), which fits the pulse between 70 and 90 s. The fifth line is for all subevents replaced by the CMT thrust mechanism. The last line is for subevent 4 replaced with a thrust mechanism as subevent 3. Observe significant misfit in the *P*-waveform data for the last two lines. Length of the plotted waveform is 90 s.

depth of ∼13 km (Supporting Information Fig. S7 and event d in Table 1). This event possibly originated at the top of the underthrust Indian Plate beneath the lesser Himalaya (Fig. 9a) and is a result of the flexural bending of the downgoing plate due to loading following the main-shock. Alternatively, as the slip vector of this earthquake matches that of subevent 2 of the main-shock, it could have occurred on the west dipping lateral ramp.

4.2 2015 April 26 aftershocks

Two major aftershocks occurred on the next day and originated within the eastern edge of the main-shock rupture (Fig. 8). Both events have predominantly thrust fault mechanism and had centroid depths of ∼14 and ∼11 km (Supporting Information Figs S8 and S9; events e and f in Fig. 8 and Table 1). The mechanism of the larger aftershock (M_w 6.9) is similar to the main-shock rupture with close match in the dip of the fault plane and centroid depth of the events. We interpret this event to have resulted from post-seismic stress adjustment at the edge of the main-shock rupture area. Modelling of source spectra (Denolle *et al.* 2015) revealed that the STF for this event has a remarkable similarity to the main-shock rupture. The smaller aftershock (M_w 5.0) occurred on a thrust fault oriented SW–NE with a steeper fault plane and shallower depth. The epicentre of the event is located at the junction between subevents 3 and 4 of the main-shock (Fig. 8). We conjecture that this event occurred on an oblique splay fault or lateral ramp on the MHT and resembles the zone of main-shock slip transfer from the MHT to the transverse structure on which subevent 4 occurred.

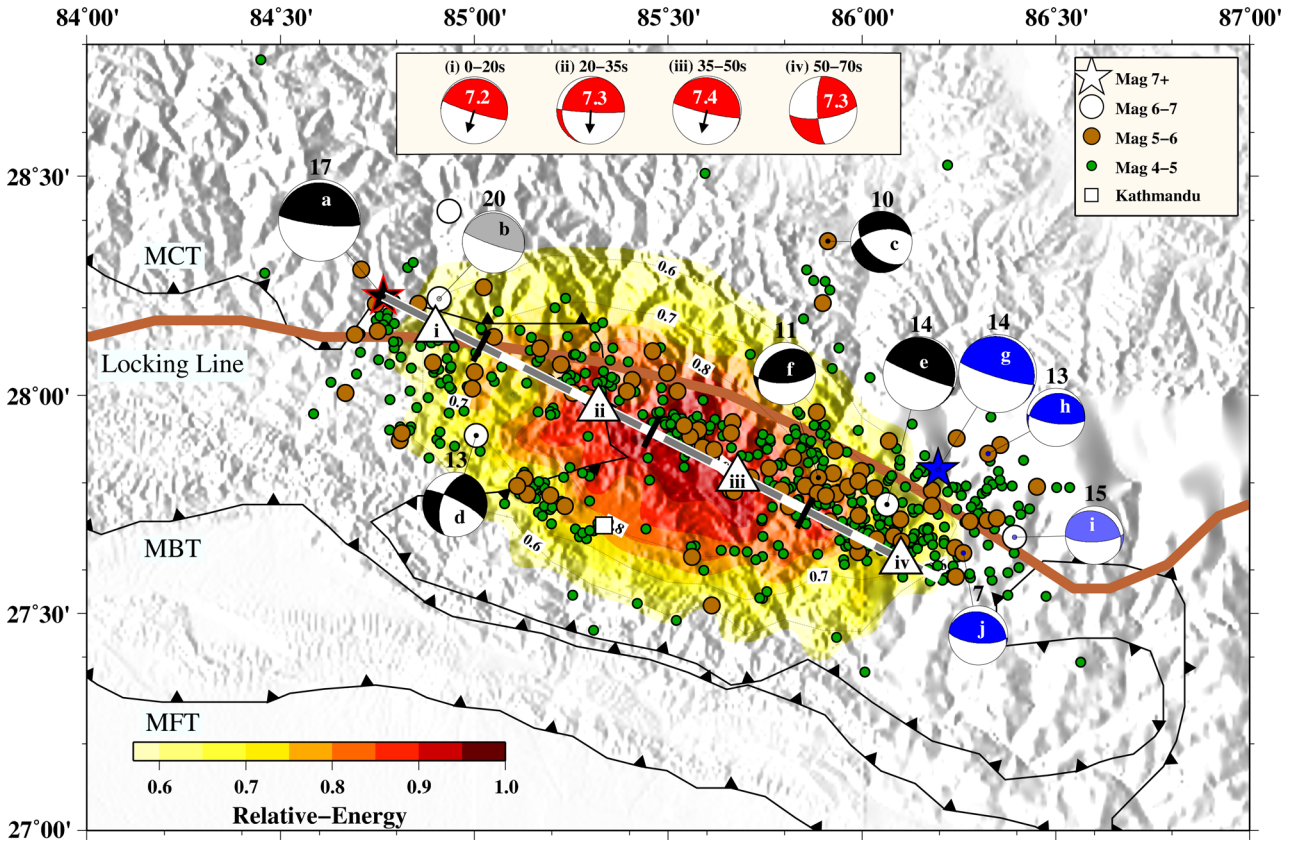

Figure 8. Map of the main-shock rupture area (taken from Fig. 2) with overlay plot of focal mechanisms computed in this study. The focal mechanism for the 2015 April 25 main-shock and the aftershocks which occurred before 2015 May 12 are coloured black. The focal mechanism for the 2015 May 12 largest aftershock and the subsequent aftershocks are coloured blue. The grey (b) and light blue (i) are mechanisms taken from GFZ and USGS, respectively. Epicentres of all aftershocks above M_w 4 are plotted as circles (see inset for colour code). The depth of the modelled earthquakes are plotted on top of the focal sphere. The line source for the main-shock is plotted as a white–grey dashed line along azimuth 117°. The main-shock subevents locations are plotted as white triangles with their corresponding focal mechanisms plotted as inset on top (red focal spheres). The STF duration for the subevents and their size (M_w) are written on top and within the focal spheres, respectively.

4.3 2015 May 12 aftershocks

The largest aftershock (M_w 7.3) occurred on 2015 May 12 and originated immediately east of the eastern end of the main-shock rupture (Fig. 8). We model this earthquake both as a centroid source (Supporting Information Fig. S10) and as a line source (Supporting Information Fig. S11) with a rupture velocity of 2.5 km $s^{-1}$and an azimuth of 150°. The rupture velocity and the orientation of the line has been obtained from back projection study (Supporting Information Fig. S3). The *P*- and *SH*-waveforms for this earthquake is dominated by long-period energy and has an impulsive initiation, unlike the main-shock (Denolle *et al.* 2015). From waveform modelling we observe that this earthquake occurred on a shallow NE dipping (∼9°) thrust fault. The STF is ∼10 s with a sharp initial rise. The centroid depth of the earthquake is modelled to be ∼15 km. The mechanism of this earthquake has remarkable similarity with the line source solution of the main-shock (Fig. 8), but the centroid depth of the event places it above the imaged MHT in this region (Monsalve *et al.* 2006) (Fig. 9). Denolle *et al.* (2015) suggested that this event possibly occurred on a shallower but similarly oriented fault as the MHT. Given the location of the epicentre (Fig. 2a) and the southward propagation of the rupture (Supporting Information Fig. S3), it is understood that this aftershock resulted in relieving residual post-seismic stresses following the main-shock rupture. Interestingly, the size of this event is larger than the Omoriś Law predicted aftershock decay magnitude. It is also worth noting that the mechanism of the M_w 6.9 aftershock which occurred a day after the main-shock, had originated within ∼10 km of the epicentre of this event and had similar depth and mechanism.

Two more aftershocks followed the M_w 7.3 aftershock within the next half an hour. The first one has a magnitude of M_w 5.5 and the second one M_w 6.3. Waveform modelling of the first aftershock revealed that the earthquake occurred on an NW dipping (∼21°) oblique thrust fault at a depth of ∼13 km (Supporting Information Fig. S12 and event h in Fig. 8 and Table 1). Due to interference of surface waves from the previous event, we could not model the body waves for the second aftershock and report the USGS mechanism (Table 1). This event occurred on a NNE dipping (∼23°) oblique thrust fault at a depth of ∼15 km. From the location, mechanism and depth of both these events, it is obvious that these occurred at the edge of the largest aftershock fault and is a result of post-seismic stress adjustments (Figs 8 and 9).

4.4 2015 May 16 aftershocks

One major aftershock (M_w 5.5) occurred four days after the largest aftershock and originated to the south of it (Fig. 8). The aftershock has a thrust mechanism, similar to the largest aftershock, but the dip of the northeast dipping plane is steeper and has a

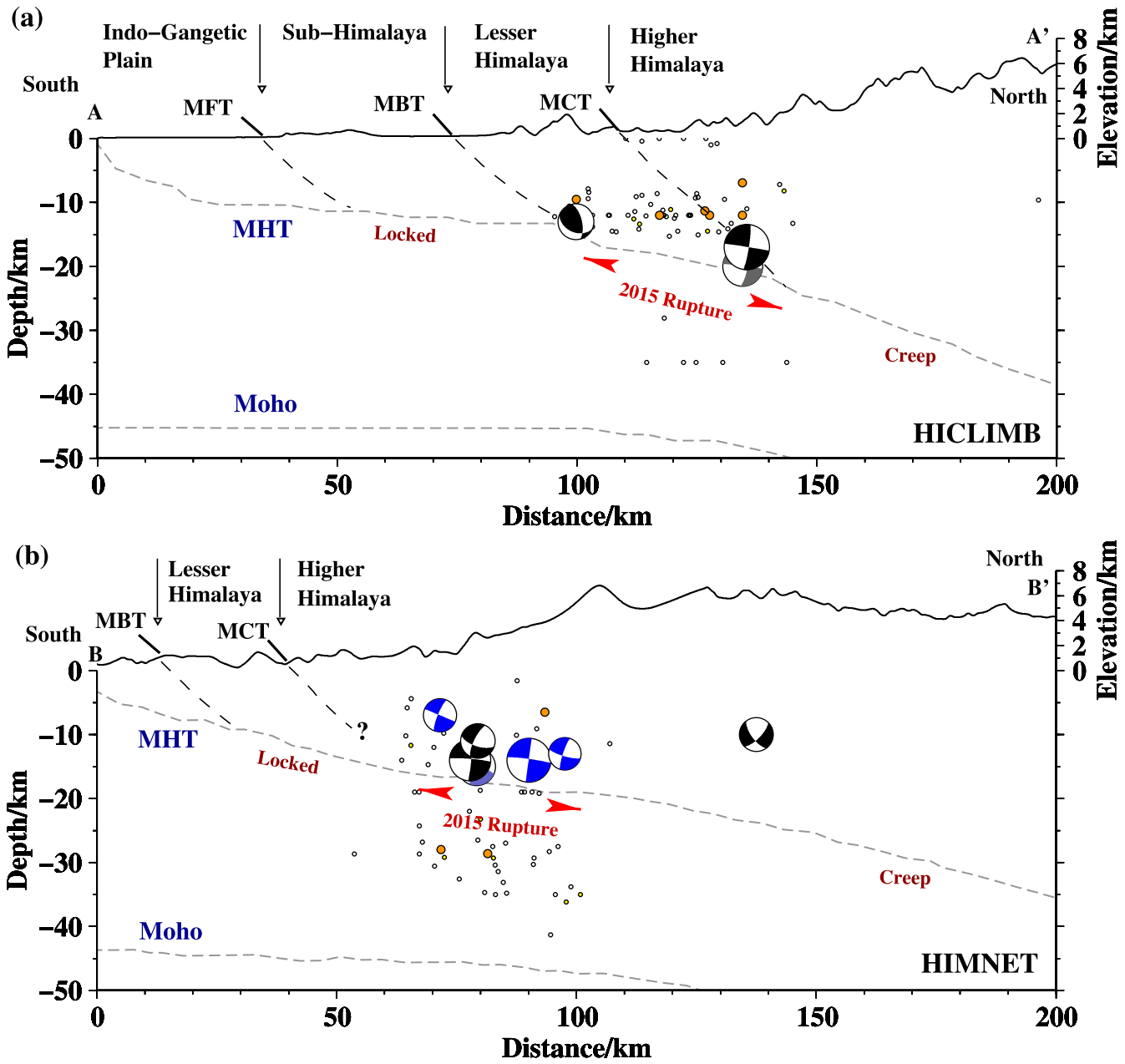

Figure 9. Plot of profiles A–A′(west) and B–B′(east) across Nepal Himalaya (marked in Fig. 1) with overlay plot of earthquake hypocentres (from Fig. 1) and focal mechanisms (from Fig. 8) within ±50 km on either side of the profile, projected onto the profile. These profiles are chosen exactly along the Hi-CLIMB (Nábělek *et al.* 2009) (A–A′ and HIMNT (Monsalve *et al.* 2006) (B–B′ seismological experiment profiles, and the geometry of the MHT and Moho has been digitized from these studies. Location of MFT, MBT and MCT, taken from Lave & Avouac (2001), has been projected onto the profile. The Gorkha main-shock and M_w 7.3 largest aftershock ruptures are observed to be confined within the two ramps on the MHT. Note the vertical exaggeration in the topographic profile.

significantly shallower centroid depth (Supporting Information Fig. S13 and event j in Table 1). This event must have occurred on a splay fault and is a result of post-seismic stress adjustment following the M_w 7.3 largest aftershock (Figs 8 and 9).

5 DEPTH SENSITIVITY OF EARTHQUAKES TO CRUSTAL VELOCITY STRUCTURE

Two major seismological experiments have been conducted in the central Nepal Himalaya in the past decade to unravel the crustal structure and seismicity. The HIMNT experiment (Schulte-Pelkum *et al.* 2005; Monsalve *et al.* 2006; Torre *et al.* 2007) spanned the eastern Nepal Himalaya and provided a one-dimensional velocity model for the region immediately east of the largest aftershock (profile B–B' in Fig. 1). The Hi-CLIMB experiment (Nábělek *et al.* 2009) spanned the central Nepal Himalaya and southern Tibet and provided a 1-D velocity structure immediately west of the epicentre of the main-shock (profile A–A′ in Fig. 1). The estimation of earthquake depth using teleseismic waveform inversion is strongly dependent on the velocity model used for the source region. We, therefore, compute the depth for all the modelled earthquakes using both these velocity models and the IASP91 model (Kennett & Engdahl 1991). The depth of these events as a function of

magnitude (Supporting Information Fig. S14) is used to observe the depth sensitivity to a chosen velocity model and any systematic errors related to the size of the event. We assume ±5 per cent uncertainty in the velocity and compute associated errors in depth. We observe that the HIMNT velocity structure is intermediate to the IASP91 and the Hi-CLIMB models and the associated depths are an average of the two models. Additionally the IASP91 and Hi-CLIMB depths fall within the uncertainty of the HIMNT model. All our waveform modelling has been done using the HIMNT velocity structure for the source region. However, for comparison, we also provide the depths for all the events for the other two velocity models (Supporting Information Fig. S14).

6 DISCUSSION

The MHT, which separates the downgoing Indian Plate from the overriding Himalayan wedge, in the India-Tibet continent-continent collisional setting, is equivalent to a subduction megathrust. From GPS geodetic measurements and geological slip rates it is known that the MHT accommodates almost half of the convergence between India and Eurasia (Bilham *et al.* 1997; Larson *et al.* 1999; Jouanne *et al.* 2004). This shortening is stored elastically within the frictionally locked zone of the MHT (between 0 and 20 km depth), while the deeper segment undergoes aseismic creep. A line of microseismicity defines the downdip edge of this frictionally locked zone and had been conjectured to be the point of initiation of mega-thrust earthquakes in the Himalaya (Chen & Molnar 1977; Bilham *et al.* 2001; Ader *et al.* 2012). This line is referred to as the 'locking line' and separates the frictionally locked-to-aseismically creeping regions on the MHT, through a downdip zone of tapered slip (Stevens & Avouac 2015). The MHT, beneath Nepal Himalaya, has been imaged using a variety of seismological techniques and is known to have a ramp-flat-ramp geometry, from surface to depth (Hirn *et al.* 1984; Monsalve *et al.* 2006; Priestley *et al.* 2008; Nábělek *et al.* 2009; Acton *et al.* 2011) (Fig. 9). The locking line has been found to coincide with the deeper crustal ramp on the MHT and the seismic-to-aseismic transition is a function of the thermo-rheological property of this detachment surface (Ader *et al.* 2012; Grandin *et al.* 2015). It is therefore understandable that the Gorkha main-shock initiated close to the downdip edge of the locked zone, underneath the Higher Himalaya and ruptured updip. The rupture propagated eastward from the epicentre, the cause for which is not clearly understood. Denolle *et al.* (2015) attributed it to the presence of transverse basement structures (e.g. the Trisouli Transform).

Our back projection results highlight that the rupture initiated ∼80 km west of Katmandu and propagated eastward for ∼150 km along an azimuth of ∼117°. This is in close agreement with previous studies of back projection (Avouac *et al.* 2015; Fan & Shearer 2015; Zhang *et al.* 2016). Distribution of high-frequency energy released during the faulting points to a multi-pulsed heterogeneous rupture process. The rupture initiated with a gradual rise in the STF, unlike most earthquakes (Denolle *et al.* 2015), but propagated with a rupture velocity of ∼3.5 km s^{-1}. This led to emanation of low-amplitude high-frequency pulses in the first ∼20 s of the fault rupture. The slow rise in the STF suggests slow slip initiation followed by dynamic weakening which resulted in a runaway rupture for the first subevent. Subsequently, the rupture velocity slowed down to ∼2.5 km s^{-1}, over the next ∼15 s, and the energy release occurred over a distributed region on the fault (Fig. 2a). Finally, the rupture speed increased to ∼3.5 km s^{-1} and split into two segments, swerving around the rupture zone of largest aftershock, which failed 18 days later. The average rupture velocity obtained from our back projection is in agreement with the ∼2.72 km s^{-1} observed by Avouac *et al.* (2015). The multi-pulsed heterogeneous rupture process with time dependent rupture velocity variation, highlighted in our study, closely matches the slow downdip rupture initiation followed by two stages of faster updip ruptures of Fan & Shearer (2015). Our results additionally show that the faster updip rupture coincides with the release of maximum energy between 30 and 50 s (Fig. 2). The extent of the ruptured segment of the MHT, obtained from our back projection result, reveal that the downdip limit of the rupture closely follows the junction between the frontal flat and the deeper steeply dipping ramp (Monsalve *et al.* 2006) underneath the Higher Himalaya (Fig. 9). The downdip arrest of the rupture is attributed to the gradient in coupling on the MHT (Ader *et al.* 2012) due to thermo-rheological effects. High-frequency radiation observed along the downdip edge of the MHT points to structural and stress heterogeneities due to the occurrence of small-to-moderate seismicity along the locking line. The updip limit of the rupture lies underneath the Lesser Himalaya at a depth of ∼10 km (Fig. 9). This has been conjectured to be either structurally controlled by the steeply dipping shallower ramp on the MHT (Elliott *et al.* 2016) or by the lower level of stresses updip of the ruptured zone. Finally, the last stage splitting of the rupture front possibly indicates a stronger patch on the MHT leading to transfer of motion onto a different fault, which has been illuminated through the multiple subevent source modelling.

Waveform inversion of the Gorkha main-shock as a line source yields a gentle north dipping (dip ∼9°) thrust fault at a depth of ∼10 km. This is in general agreement with the centroid moment tensor solution. However, the steeper dip of the fault plane possibly indicates lateral variation in the dip of the ruptured segment of the MHT. The multiple subevent inversion is built on this line source model and is coupled with the high-frequency rupture propagation to illuminate the detailed geometry of the faulted segment of the MHT. In order to compare this result with the back projection, we plot the location of the four subevents in Fig. 8 and the associated focal mechanism as inset plots on the top of the map. The location of the subevents are estimated using the rupture velocity of 2.3 km s^{-1} (used in the line source modelling) and is plotted on the line source with azimuth of 117°. Subevents 1 and 3 occurred on the shallow north dipping flat segment of the MHT, with pure thrust motion. The dip of these segments are ∼6° and ∼7°, respectively, and matches well with the dip of the MHT, derived from geology (Schelling & Arita 1991) and suggested from receiver function studies (Nábělek *et al.* 2009). The initial pulse modelled in subevents 1 and the largest amplitude modelled in subevent 3 possibly controls the centroid and line source mechanisms of the main-shock. This explains the observed similarity of the centroid and line source mechanism of the main-shock to those of subevents 1 and 3. Subevent 2 occurred on a ∼west dipping, steeper fault plane (dip ∼18°) with oblique thrust motion. This points to a lateral ramp on the MHT (Berger *et al.* 2004) over which the rupture propagated eastwards. The SSW–NNE zone of aftershock concentration west of Katmandu (Adhikari *et al.* 2015) possibly delineates the position of the lateral ramp, with transfer of stress in the overlying strata subsequent to rupture on a steeply dipping segment of the MHT ramp. The slip vectors for all the three subevents are consistently oriented to the S–SSW and results from overthrusting of the Himalayan wedge over the Indian Plate along the MHT. The most significant observation in the multiple event modelling of the main-shock comes from subevent 4, which is observed to be an oblique strike-slip earthquake on a transverse structure.

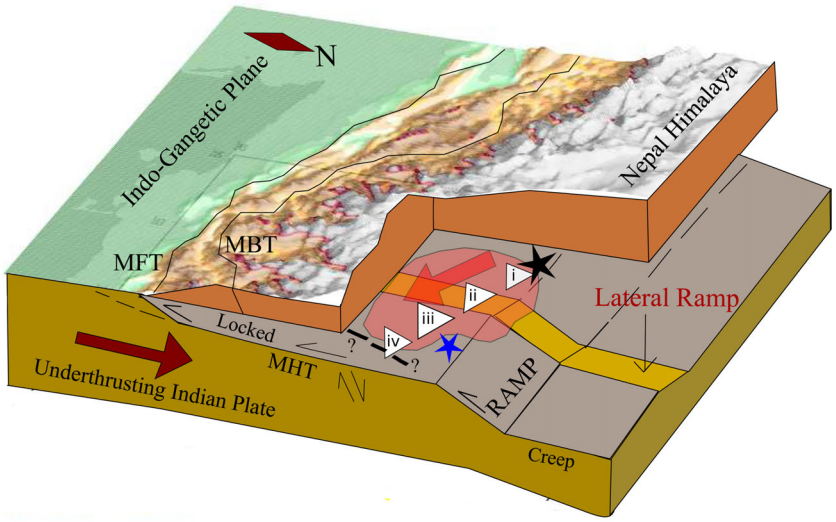

Figure 10. Schematic block diagram depicting the fault rupture area and location of four subevents of the Gorkha earthquake in context of the ramp-flat-ramp geometry and lateral ramp on the MHT.

Combining the spatiotemporal evolution of these subevents and the high-frequency rupture propagation reveal that the faulting initiated in the west and propagated eastward on the MHT flat between 0–20 s, with the tip of the rupture propagating at ∼3.5 km s^{-1}. It then encountered the lateral ramp on the MHT and went over it between 20–35 s. This possibly led to the observed slowdown in the rupture speed to ∼2.5 km s^{-1}. Once the rupture front overcame the lateral ramp, it propagated further eastward at a velocity of ∼3.5 km s^{-1} and resulted in the maximum energy release (subevent 3 with M_w 7.4), surrounding the centroid location of the earthquake fault. The heterogeneity on the MHT in the form of the lateral ramp produced the observed pulsating nature of the rupture observed in the back projection results (Fig. 2a and Supporting Information Movie S1). In the final stage of the rupture, the eastward motion on the MHT was transferred onto a steeply dipping strike-slip fault, which ruptured in subevent 4. Dip of the nodal planes do not match the dip of the MHT and therefore must be a transverse structure either at the base of the Himalayan wedge or on the top of the downgoing Indian Plate. If we choose the N–S plane of subevent 4 as the fault plane, the rupture occurred through left-lateral strike-slip motion, with the slip vector pointing to the S. This is consistent with the slip vectors of the first three subevents and points to transfer of motion onto an oblique structure, which possibly acted as a barrier in limiting the along strike propagation of rupture further to the east. We propose this to be one of the plausible explanations for along-strike arrest of thrust faulting on the MHT. Analogous example of strike-slip faults ending in thrust motion has been observed in the Kopeh Dagh Mountains in NE Iran (Hollingsworth *et al.* 2006) and in Mongolia (Bayasgalan *et al.* 1999).

The eastward propagation of the main-shock rupture led to enhanced stresses on the eastern segment of the MHT and resulted in a large number of aftershocks east of the main-shock rupture area (Fig 1). This includes the largest M_w 7.3 aftershock which ruptured a shallow NNE dipping thrust fault with similar motion as the main-shock. From back projection of high-frequency energy for this aftershock we observe that the rupture initiated on the eastern edge of the main-shock and close to the locking line and propagated SSE. The trend of one of the nodal planes of the last stage main-shock rupture (subevent 4) matches closely with the distribution of high-frequency generation on the aftershock fault (Supporting Information Fig. S2). Interestingly the dip of the largest aftershock thrust fault plane matches the dip of the MHT, but the modelled depth of the aftershock puts it within the Himalayan wedge, ∼5 km above the MHT (Fig. 9). Denolle *et al.* (2015) suggested that this event occurred above the Plate interface on a parallel fault, proposed earlier from structural studies. However, it is worth noting that the presence of the lateral ramp, encountered by the main-shock rupture, shallows the MHT by almost the same amount to the east. The largest aftershock, with allowance for uncertainty in depth, could therefore, lie on the shallower eastward segment of the MHT. This led to the release of the majority of the stresses built-up on this segment of the MHT due to the splitting of the last stage main-shock rupture and its subsequent arrest on a transverse fault. Alternatively the main-shock rupture could have ran into a patch of aseismic creep as proposed by Gualandi *et al.* (2016) through study of post-seismic slip using GPS geodetic data. From the distribution (Fig. 1) and source mechanism of the smaller aftershocks (Fig. 8), east of the main-shock rupture, it is evident that these resulted in relaxation of the residual stresses in the volume of rocks surrounding the main-shock and the largest aftershock. The along dip extent of the rupture (Fig. 9) and distribution of aftershocks (Figs 1 and 8) independently delineates the northern and southern edges of the main-shock rupture zone and confirms that it was confined downdip by the seismic-aseismic transition on the mid-crustal MHT ramp and updip by the shallow frontal ramp (Figs 9 and 10). Structural control on the main-shock rupture zone has also been suggested from three-dimensional construction of the ruptured segment on the MHT using structural cross-section and geological information (Hubbard *et al.* 2016).

Finally, the source mechanism of the smaller aftershocks highlight two important processes associated with plate boundary earthquakes in the Himalaya. First, is the transfer of stresses from the plate boundary to the top of the downgoing Indian Plate. This is illustrated by the occurrence of normal fault underneath the lesser Himalaya, on top of the downgoing Indian Plate, due to flexural bending of the plate (Figs 8 and 9). This is also observed in outer rise of subduction zones (Craig *et al.* 2014). The second is the normal fault within the Tethyan Himalaya, north of the main-shock

rupture (Figs 8 and 9). This is caused by the extension in the north due to the sudden southward slip of the Himalayan Mountains over the Indian Plate in the Gorkha main-shock. It also results in the observed lowering of the topography of the high mountains during co-seismic slip of the main-shock (Elliott *et al.* 2016).

7 CONCLUSIONS

We use high-frequency back projection on broad-band data from multiple teleseismic arrays to study the spatiotemporal evolution of the Gorkha main-shock and its largest aftershock. Based on the results of the back projection, we parameterize the main-shock and the largest aftershock as propagating line sources and model their source mechanism using P and *SH*-waveform data from GDSN stations. The observed heterogeneity in the main-shock rupture process prompted us to further parameterize the main-shock into four subevents and invert these independently as centroid sources to highlight the lateral variation on the main-shock fault. Finally, we model the source mechanism of six larger aftershocks, which occurred within a month of the main-shock, using centroid moment tensor inversion. These together provide a comprehensive understanding of the geometry and kinematics of faulting of the 2015 Gorkha earthquake and its aftershocks.

The main conclusions of our study are as follows:

(1) The main-shock rupture initiated ∼80 km west of Katmandu, at the downdip edge of the locked segment of the MHT and propagated eastwards. The cumulative energy released during the earthquake occurred over a fault area of ∼150 km by ∼70 km. From the integrated STF we observe that the rupture occurred over ∼70 s duration, and had three distinct peaks at ∼30, ∼45 and ∼60 s.

(2) The rupture initiated with a slow buildup in the STF and then propagated at a velocity of ∼3.5 km s^{-1}. This emanated low-amplitude high-frequency energy observed in the first 20 s of the waveform. Multiple subevent modelling reveal that the faulting occurred on the MHT flat, NW of Katmandu (dip ∼6° N) and produced a centroid source of M_w 7.2.

(3) Between 20 and 35 s the faulting occurred on a W dipping (∼18°WNW) lateral ramp on the MHT, which resulted in the observed slowdown in the rupture velocity ∼2.5 km s^{-1}. This produced a centroid source of M_w 7.3.

(4) The largest subevent (M_w 7.4) occurred between 35–50 s and ruptured the MHT flat (dip ∼7° N) east of the lateral ramp. The rupture velocity increased to ∼3.5 km s^{-1}. The mechanisms of subevents 1 and 3 have a close resemblance to the centroid and line source mechanism of the main-shock, confirming that the initial pulse and the largest amplitude on teleseismic body waveforms controlled the centroid and line source mechanisms. Moreover, the slip vectors of the first three subevents points to the S-SSE in agreement to the southward slip of the Himalaya over the Indian Plate.

(5) Between 50 and 70 s the rupture split into two segments swerving around the source region of the largest aftershock and ruptured a steeply dipping transverse fault with left-lateral strike-slip motion. This possibly arrested the main-shock rupture from propagating further eastward on the MHT.

(6) The heightened stresses east of the main-shock fault resulted in the largest aftershock which ruptured the MHT flat (dip ∼9°NE) immediately east of the main-shock. The rupture initiating close to the locking line and propagated in the SSE direction.

(7) The smaller aftershocks resulted in relaxation of the residual stresses in the volume of rocks surrounding the main-shock and the largest aftershocks. Source mechanisms highlight stress adjustment at the edges of the main-shock and aftershock rupture areas, transfer of stresses from the plate boundary to the top of the downgoing Indian Plate and extensional faulting within the hanging wall of the MHT, underneath the Tethyan Himalaya.

The slip deficit of ∼4 m, which had accumulated on MHT since the 1833 (M ∼7.5) earthquake, got released in the Gorkha main-shock and its largest aftershock. However, the rupture of the Gorkha main-shock, and possibly that of the 1833 earthquake, stopped ∼10 km below the surface. This has led to transfer of two cycles of ∼4 m potential slip onto the frictionally locked updip segment of the MHT. This will result in enhanced probability of failure both updip and west of the Gorkha earthquake rupture zone, where the last known megathrust earthquake occurred in 1505 with an estimated slip of ∼20 m (Kumar *et al.* 2006). This knowledge should be incorporated in future seismic hazard assessment of Nepal Himalaya and northern India.

ACKNOWLEDGEMENTS

Seismograms for a part of this study have been downloaded from IRIS-DMC (www.iris.edu/dms/dmc/). We acknowledge the following FDSN network operators for the data: AF AK AT AU AV CH CN CZ DK EI FR G GB GE GR GT HL IC II IM IU JP KG KN KO KR KZ LX MI MN MY NJ NL NO OE PL PM PS RO SS SY TA TT UK US XI2010 XS2008 ZC2008 ZE2008. Data pre-processing and part of the analysis were performed using Seismic Analysis Code, version 100 (Goldstein *et al.* 2003). All plots were made using the Generic Mapping Tools version 4.0 (www.soest.hawaii.edu/gmt; Wessel & Smith (1998). SKS acknowledges CSIR-JRF fellowship; and AK and SM acknowledges IISER Kolkata Annual Research Funds (ARF). SD acknowledges support from Vice-Chairman BSDMA. This work was partially supported by the DfID under the Science for Humanitarian Emergencies and Resilience Programme (project code 201884), an NERC emergency grant, and through the Earthquakes Without Frontiers (EWF) programme.

REFERENCES

Acton, C., Priestley, K., Mitra, S. & Gaur, V., 2011. Crustal structure of the Darjeeling–Sikkim Himalaya and southern Tibet, *Geophys. J. Int.,* **184,** 829–852.

Ader, T. *et al.*, 2012. Convergence rate across the Nepal Himalaya and interseismic coupling on the Main Himalayan Thrust: implications for seismic hazard, *J. geophys. Res.,* **117**(B4), B04403, doi:10.1029/2011JB009071.

Adhikari, L. *et al.*, 2015. The aftershock sequence of the 2015 April 25 Gorkha–Nepal earthquake, *Geophys. J. Int.,* **203**(3), 2119–2124.

Ambraseys, N. & Douglas, J., 2004. Magnitude calibration of north Indian earthquakes, *Geophys. J. Int.,* **159,** 165–206.

Avouac, J.-P., Meng, L., Wei, S., Wang, T. & Ampuero, J.-P., 2015. Lower edge of locked Main Himalayan Thrust unzipped by the 2015 Gorkha earthquake, *Nat. Geosci.,* **8,** 708–711.

Bayasgalan, A., Jackson, J., Ritz, J.-F. & Carretier, S., 1999. Field examples of strike-slip fault terminations in Mongolia and their tectonic significance, *Tectonics,* **18**(3), 394–411.

Berberian, M., Jackson, J., Qorashi, M., Khatib, M., Priestley, K., Talebian, T. & Ghafuri-Ashtiani, M., 1999. The 1997 May 10 Zirkuh (Qa'enat) earthquake (M_w = 7.2): faulting along the Sistan suture zone of eastern Iran, *Geophys. J. Int.,* **136,** 671–694.

Berger, A., Jouanne, F., Hassani, R. & Mugnier, J.L., 2004. Modelling the spatial distribution of present-day deformation in Nepal: how cylindrical is the Main Himalayan Thrust in Nepal?, *Geophys. J. Int.,* **156,** 94–114.

Bilham, R. & Wallace, K., 2005. Future $M_w > 8$ earthquakes in the Himalaya: implications from the 26 Dec 2004 $M_w = 9.0$ earthquake on India's eastern plate margin, *Geol. Surv. India Spl. Pub.,* **85,** 1–14.

Bilham, R., Larson, K. & Freymueller, J., 1997. GPS measurements of present-day convergence across the Nepal Himalaya, *Nature,* **386**(6620), 61–64.

Bilham, R., Gaur, V. & Molnar, P., 2001. Himalayan seismic hazard, *Science,* **293,** 1442–1444.

Chen, W.-P. & Molnar, P., 1977. Seismic moments of major earthquakes and the average rate of slip in Central Asia, *J. geophys. Res.,* **82,** 2945–2969.

Craig, T., Copley, A. & Middleton, T., 2014. Constraining fault friction in oceanic lithosphere using the dip angles of newly-formed faults at outer rises, *Earth planet. Sci. Lett.,* **392,** 94–99.

Craig, T.J., Copley, A. & Jackson, J., 2012. Thermal and tectonic consequences of India underthrusting Tibet, *Earth planet. Sci. Lett.,* **353–354,** 231–239.

Denolle, M.A., Fan, W. & Shearer, P.M., 2015. Dynamics of the 2015 M7.8 Nepal earthquake, *Geophys. Res. Lett.,* **42**(18), 7467–7475.

Elliott, J., Jolivet, R., González, P., Avouac, J.-P., Hollingsworth, J., Searle, M. & Stevens, V., 2016. Himalayan megathrust geometry and relation to topography revealed by the Gorkha earthquake, *Nat. Geosci.,* **9,** 174–180.

Fan, W. & Shearer, P.M., 2015. Detailed rupture imaging of the 25 April 2015 Nepal earthquake using teleseismic*P* waves, *Geophys. Res. Lett.*, **42**(14), 5744–5752.

Galetzka, J. *et al.*, 2015. Slip pulse and resonance of the Kathmandu basin during the 2015 Gorkha earthquake, Nepal, *Science,* **349**(6252), 1091–1095.

Goldstein, P., Dodge, D., Firpo, M. & Minner, L., 2003. Sac2000: Signal processing and analysis tools for seismologists and engineers, in *The IASPEI International Handbook of Earthquake and Engineering Seismology,* eds Lee, W., Kanamori, H., Jennings, P. & Kisslinger, C., Academic Press.

Grandin, R., Vallée, M., Satriano, C., Lacassin, R., Klinger, Y., Simoes, M. & Bollinger, L., 2015. Rupture process of the $M_w = 7.9$ 2015 Gorkha earthquake (Nepal): insights into Himalayan megathrust segmentation, *Geophys. Res. Lett.,* **42**(20), 8373–8382.

Gualandi, A. *et al.*, 2016. Pre-and post-seismic deformation related to the 2015, M_w7.8 Gorkha earthquake, Nepal, *Tectonophysics,* doi:10.1016/j.tecto.2016.06.014.

Hayes, G.P., Bergman, E., Johnson, K.L., Benz, H.M., Brown, L. & Meltzer, A.S., 2013. Seismotectonic framework of the 2010 February 27 M_w 8.8 Maule, Chile earthquake sequence, *Geophys. J. Int.,* **195,** 1034–1051.

Hirn, A. *et al.*, 1984. Crustal structure and variability of the Himalayan border of Tibet, *Nature,* **307**(5946), 23–25.

Hollingsworth, J., Jackson, J., Walker, R., Gheitanchi, M.R. & Bolourchi, M.J., 2006. Strike-slip faulting, rotation, and along-strike elongation in the Kopeh Dagh mountains, NE Iran, *Geophys. J. Int.,* **166**(3), 1161–1177.

Hubbard, J., Almeida, R., Foster, A., Sapkota, S.N., Bürgi, P. & Tapponnier, P., 2016. Structural segmentation controlled the 2015 M_w 7.8 Gorkha earthquake rupture in Nepal, *Geology,* **44**(8), 639–642.

Jouanne, F., Mugnier, J.L., Gamond, J.F., Le Fort, P., Pandey, M.R., Bollinger, L., Flouzat, M. & Avouac, J.P., 2004. Current shortening across the Himalayas of Nepal, *Geophys. J. Int.,* **157**(1), 1–14.

Kennett, B. & Engdahl, E., 1991. Traveltimes for global earthquake location and phase identification, *Geophys. J. Int.,* **105**(2), 429–465.

Kiser, E. & Ishii, M., 2012. Combining seismic arrays to image the high frequency characteristics of large earthquakes, *Geophys. J. Int.,* **188**(3), 1117–1128.

Kiser, E., Ishii, M., Langmuir, C., Shearer, P. & Hirose, H., 2011. Insights into the mechanism of intermediate-depth earthquakes from source properties as imaged by back projection of multiple seismic phases, *J. geophys. Res.,* **116**(B6), doi:10.1029/2010JB007831.

Kumar, A., Mitra, S. & Suresh, G., 2015. Seismotectonics of the eastern Himalayan system and Indo-Burman plate boundary systems, *Tectonics,* **34**(11), 2279–2295.

Kumar, S., Wesnousky, S.G., Rockwell, T.K., Briggs, R.W., Thakur, V.C. & Jayangondaperumal, R., 2006. Paleoseismic evidence of great surface rupture earthquakes along the Indian Himalaya, *J. geophys. Res.,* **111**(B3), B03304, doi:10.1029/2004JB003309.

Larson, K.M., Bürgmann, R., Bilham, R. & Freymueller, J.T., 1999. Kinematics of the India-Eurasia collision zone from GPS measurements, *J. geophys. Res.,* **104**(B1), 1077–1093.

Lave, J. & Avouac, J., 2001. Fluvial incision and tectonic uplift across the Himalayas of central Nepal, *J. geophys. Res.,* **106**(11), 26 561–26 591.

McCaffrey, R. & Abers, J., 1988. SYN3: A program for inversion of teleseismic body wave form on microcomputers, Tech. Rep. AFGL-TR-0099, Air Force Geophysical Laboratory, Hanscomb Air Force Base, Massachussets.

McCaffrey, R. & Nabelek, F., 1987. Earthquakes, gravity and the origin of the Bali Basin: an example of a nascent continental fold-and-thrust belt, *J. geophys. Res.,* **92,** 441–460.

McKenzie, D. & Jackson, J., 2012. Tsunami earthquake generation by the release of gravitational potential energy, *Earth planet. Sci. Lett.,* **345,** 1–8.

Meng, L., Zhang, A. & Yagi, Y., 2016. Improving back projection imaging with a novel physics-based aftershock calibration approach: a case study of the 2015 Gorkha earthquake, *Geophys. Res. Lett.,* **43**(2), 628–636.

Mitra, S., Paul, H., Kumar, A., Singh, S.K., Dey, S. & Powali, D., 2015. The 25 April 2015 Nepal earthquake and its aftershocks, *Curr. Sci.,* **108**(10), 1938–1943.

Monsalve, G., Sheehan, A., Schulte-Pelkum, V., Rajaure, S., Pandey, M.R. & Wu, F., 2006. Seismicity and one-dimensional velocity structure of the himalayan collision zone: earthquakes in the crust and upper mantle, *J. geophys. Res.,* **111,** B10301, doi:10.1029/2005JB004062.

Nabelek, J., 1984. Determination of earthquake source parameters from inversion of body waves, *PhD thesis,* Massachusetts Institute of Technology.

Nábělek, J. *et al.*, 2009. Underplating in the Himalaya-Tibet collision zone revealed by the hi-climb experiment, *Science,* **325**(5946), 1371–1374.

Paul, H., Mitra, S., Bhattacharya, S. & Suresh, G., 2015. Active transverse faulting within underthrust Indian crust beneath the Sikkim Himalaya, *Geophys. J. Int.,* **201**(2), 1070–1081.

Priestley, K., Jackson, J. & Mckenzie, D., 2008. Lithospheric structure and deep earthquakes beneath India, the Himalaya and southern Tibet, *Geophys. J. Int.,* **172,** 345–362.

Sapkota, S., Bollinger, L., Klinger, Y., Tapponnier, P., Gaudemer, Y. & Tiwari, D., 2013. Primary surface ruptures of the great Himalayan earthquakes in 1934 and 1255, *Nat. Geosci.,* **6**(1), 71–76.

Schelling, D. & Arita, K., 1991. Thrust tectonics, crustal shortening, and the structure of the far-eastern Nepal Himalaya, *Tectonics,* **10**(5), 851–862.

Schulte-Pelkum, V., Monsalve, G., Sheehan, A., Pandey, M.R., Sapkota, S., Bilham, R. & Wu, F., 2005. Imaging the Indian Subcontinent beneath the Himalaya, *Nature,* **435,** 1222–1225.

Stevens, V.L. & Avouac, J.P., 2015. Interseismic coupling on the main himalayan thrust, *Geophy. Res. Lett.,* **42**(14), 5828–5837.

Torre, T.L., Monsalve, G., Sheehan, A.F., Sapkota, S. & Wu, F., 2007. Earthquake processes of the Himalayan collision zone in eastern Nepal and the southern Tibetan Plateau, *Geophys. J. Int.,* **171,** 718–738.

Wessel, P. & Smith, W. H.F., 1998. New, improved version of the generic mapping tools released, *EOS, Trans. Am. geophys. Un.,* **79,** 579.

Yagi, Y. & Okuwaki, R., 2015. Integrated seismic source model of the 2015 Gorkha, Nepal, earthquake, *Geophys. Res. Lett.,* **42**(15), 6229–6235.

Zhang, H., van der Lee, S. & Ge, Z., 2016. Multi-array rupture imaging of the devastating 2015 Gorkha, Nepal earthquake sequence, *Geophys. Res. Lett.,* **43,** 584–591.

SUPPORTING INFORMATION

Supplementary data are available at *GJIRAS* online.

Movie S1. Spatiotemporal evolution of the Gorkha main-shock rupture. The maximum amplitude at every 1 s time frame are contoured and the energy is normalized in each time frame. Note the eastward propagation of rupture in multiple phases and the last stage rupture both updip and downdip on the MHT.

Figure S2. (a) Comparison plot of the back projection result of the Gorkha main-shock using multiple networks (AU, EU and JP), plotted as circles, and the reference Australian Network (AU), plotted as squares. Details of the figure are same as Fig. 2(a). (b) Comparison of the integrated source time function for the multiple networks with each individual network (see inset for colour code of network). (c) Comparison of rupture velocity for the multiple networks (AU, EU and JP), plotted as circles, and the reference Australian Network (AU), plotted as squares. Details of the figure are same as Fig. 2(c).

Figure S3. Plot of *P*-wave high-frequency (0.5–2.0 Hz) back projection result for the 2015 May 12 largest (M_w 7.3) aftershock. The rest of the caption is same as Fig. 2.

Figure S4. Waveform inversion result for a centroid source for the main-shock (labelled a in Table 1). Rest of the figure caption is same as Fig. 3.

Figure S5. *P*-waveform inversion result for main-shock subevent 1 for 25 s window. Rest of the figure caption is same as Fig. 3.

Figure S6. Waveform inversion result for a centroid source for the aftershock (labelled c in Table 1). Rest of the figure caption is same as Fig. 3.

Figure S7. Waveform inversion result for a centroid source for the aftershock (labelled d in Table 1). Rest of the figure caption is same as Fig. 3.

Figure S8. Waveform inversion result for a centroid source for the aftershock (labelled e in Table 1). Rest of the figure caption is same as Fig. 3.

Figure S9. Waveform inversion result for a centroid source for the aftershock (labelled f in Table 1). Rest of the figure caption is same as Fig. 3.

Figure S10. Waveform inversion result for a centroid source for the aftershock (labelled g in Table 1). Rest of the figure caption is same as Fig. 3.

Figure S11. Waveform inversion result for a line source for the largest aftershock (M_w 7.3) which occurred on 2015 May 12. Rest of the figure caption is same as Fig. 3.

Figure S12. Waveform inversion result for a centroid source for the aftershock (labelled h in Table 1). Rest of the figure caption is same as Fig. 3.

Figure S13. Waveform inversion result for a centroid source for the aftershock (labelled j in Table 1). Rest of the figure caption is same as Fig. 3.

Figure S14. Comparison plot of modelled depths along with uncertainties for the Gorkha main-shock and aftershocks for three velocity models (IASP91, HIMNT and Hi-CLIMB). The corresponding velocity models have been plotted in the inset for reference. The HIMNT velocity model is intermediate between the three and its uncertainties span the values obtained from the other two models. We therefore use the HIMNT model for the waveform inversions.

Please note: Oxford University Press is not responsible for the content or functionality of any supporting materials supplied by the authors. Any queries (other than missing material) should be directed to the corresponding author for the paper.